RSC Advances

PAPER

View Article Online
View Journal | View Issue

Cite this: RSC Adv., 2015, 5, 34157

Water steam effect during high CO_2 chemisorption in lithium cuprate (Li_2CuO_2) at moderate temperatures: experimental and theoretical evidence

Hugo A. Lara-García,[a] Brenda Alcántar-Vázquez,[a] Yuhua Duan[b] and Heriberto Pfeiffer*[a]

Li_2CuO_2 was evaluated as a CO_2 captor at moderate temperatures, using water vapor in the gas flow. Different water vapor sorption experiments were performed using N_2 or CO_2 as carrier gases. If N_2 was used as carrier gas, it was evidenced that Li_2CuO_2 is able to trap water physically and chemically, producing in the second case Li–OH superficial species. Moreover, when CO_2 was used as carrier gas, Li_2CuO_2 continued trapping water, as in the previous case, but in this case CO_2 was mainly trapped, forming Li_2CO_3 and CuO phases. Additionally, the microstructure changes importantly when CO_2 and H_2O are chemically trapped in Li_2CuO_2. Li_2CO_3 and CuO seemed to segregate changing the morphology and the specific surface area. The Li_2CuO_2 sample was able to capture up to 6.7 mmoles of CO_2 per gram of ceramic at 80 °C, a considerably high CO_2 amount. Furthermore, all these experiments were theoretically supported by different thermodynamic calculations. Experimental and theoretical results show that H_2O acts as a catalytic intermediate, diminishing the activation energy of the whole CO_2 chemisorption process. Therefore, the presence of water vapor strongly favored the CO_2 chemisorption on Li_2CuO_2 at moderate temperatures (30–80 °C).

Received 27th February 2015
Accepted 7th April 2015

DOI: 10.1039/c5ra03580e

www.rsc.org/advances

1. Introduction

Nowadays, a main contributor to global warming and climate change problems is believed to be carbon dioxide (CO_2) produced due human activities, mainly from industrial gas streams.[1,2] It is necessary to reduce the amounts of CO_2 gas produced. Numerous techniques (*e.g.*, adsorption, chemisorption, cryogenic distillation, membrane separation) have been applied in order to reduce the amount of CO_2 emitted from large exhaust sources such as fossil fuel power plants, cement industries, iron and steel mills and other industry sectors which account for about 60% of total CO_2 emissions.[1,3]

Many studies have been focused on the development of solid CO_2 sorbents with high CO_2 sorption capacity and kinetics, good selectivity at low (30–200 °C), moderate (200–400 °C) or high temperature (>400 °C) and excellent regeneration ability.[2] In that way, some materials have been tested as CO_2 captors at low and moderate temperatures, such as carbon-based adsorbents, zeolites, hydrotalcites-like materials, metal–organic frameworks (MOFs), CaO-based sorbents and alkaline ceramics, among others.[2,4,5] Among alkaline ceramics, lithium and sodium ceramics are the most studied at a wide temperature range (30–800 °C), for example zirconates, aluminates and silicates.[6–34]

In addition, typical flow gas composition post-combustion contain approximately 65–75% N_2, 7–15% CO_2, 2–12% O_2, 5–15% H_2O, and smaller concentrations of other polluting species.[3] Since water vapor is present in the flue gas post-combustion some works have been performed to understand the capture of CO_2 in different CO_2–H_2O compositions. Particularly, among alkaline and earth alkaline ceramics, there are a few papers showing the effects of water vapor during de CO_2 absorption at low temperatures (30–80 °C).[34–40] Most of these works mention that water vapor improve the CO_2 chemisorption due to the superficial hydroxylation processes. For example, it was recently published that CO_2 capture in Li_4SiO_4 is improved under the water vapor presence because the presence of steam enhances Li^{1+} diffusion and reactivity between Li_4SiO_4 and CO_2.[40]

On the other hand, lithium cuprate (Li_2CuO_2) presents interesting electronic and magnetic properties, so it has been used for different electrical applications such as cathodes for lithium-ion batteries and as a superconductor material, owing to the excellent lithium diffusion.[41–44] Some of these diffusion

[a]Instituto de Investigaciones en Materiales, Universidad Nacional Autónoma de México, Circuito Exterior s/n Cd. Universitaria, Del. Coyoacán, CP 04510, México DF, Mexico. E-mail: pfeiffer@iim.unam.mx; Fax: +52 (55) 5616 1371; Tel: +52 (55) 5622 46 27

[b]National Energy Technology Laboratory, United States Department of Energy, 626 Cochrans Mill Road, Pittsburgh, Pennsylvania 15236, USA

properties have been attributed to the Li_2CuO_2 layered crystalline structure, where the lithium atoms are located between the layers (Fig. 1).[45] The Li_2CuO_2 presents an orthorhombic phase with the following unit cell parameters: $a = 3.655$ Å, $b = 2.860$ Å, $c = 9.377$ Å and $Z = 2$.

Recently, it has been reported that the Li_2CuO_2 is able to trap CO_2 in a wide range of temperatures (120–650 °C).[46–49] These papers show that Li_2CuO_2 is able to chemisorb CO_2, where the maximum theoretical CO_2 chemisorption capacity is 9.11 mmoles of CO_2 per gram of Li_2CuO_2 (0.401 g_{CO_2} per $g_{ceramic}$). These reports show that Li_2CuO_2 begins to react with CO_2 at around 120 °C in dry conditions. Thus, the presence of water vapor may improve the CO_2 chemisorption at low temperatures in this lithium ceramic. Therefore, the aim of the work reported here was to study the CO_2–H_2O capture process in Li_2CuO_2 at a low temperature range (30–80 °C).

2. Experimental section

Lithium cuprate (Li_2CuO_2) was synthesized by solid-state method. Initially, lithium oxide (Li_2O, Aldrich) and copper oxide (CuO, Across Organics) were mixed mechanically, in order to get a good homogeneity of the reagents. The mixtures were prepared using a lithium excess of 10 wt%, based on the stoichiometric lithium content on Li_2CuO_2, as lithium tends to sublimate during high thermal treatments. Then, the powders were calcined at 800 °C for 6 h in air.

A diffractometer (Siemens D-5000) coupled to an X-ray tube was used to identify the phases obtained. The phase was identified using the Joint Committee Powder Diffraction Standards (JCPDS) files. The microstructural characteristics of the Li_2CuO_2 sample was determined *via* N_2 adsorption–desorption and scanning electron microscopy (SEM). N_2 adsorption (Bel-Japan Minisorp II) was used to determine the sample surface area using the BET model. Then, the sample morphology was analyzed by SEM, which was performed on a JEOL JMS-7600F.

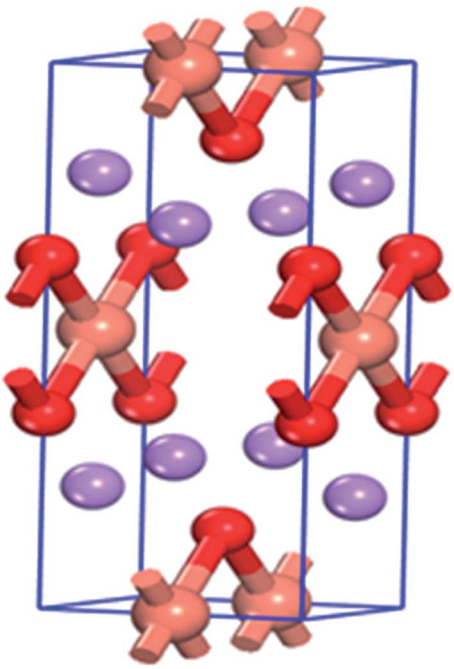

Fig. 1 Crystal structure of Li_2CuO_2 in space group *Immm* (no. 71). Red stands for oxygen, purple stands for lithium, and orange stands for copper.

The CO_2–H_2O sorption process was evaluated dynamic and isothermally in a humidity-controlled thermobalance (TA Instruments, model Q5000SA) at different temperatures and relative humidity (RH). The experiments were performed using distilled water and two different flow gases: nitrogen (N_2, Praxair grade 4.8) or carbon dioxide (CO_2, Praxair grade 3.0). The total flow gas used in all the experiments was 100 mL min^{-1} and the RH percentages were controlled automatically by the Q5000SA equipment. Dynamic water vapor sorption/desorption experiments were generated at different temperatures (between 30 and 80 °C), varying the RH from 0 to 80% (sorption) and then from 80 to 0% (desorption) at a rate of 0.5% per min, using 100 mL of N_2 or CO_2 as flow gas during the entire experiment. Additionally, different isothermal experiments were performed at specific temperatures (20, 40, 60 and 80 °C) setting the RH at different values (20, 40, 60 and 80%) for 180 min, using CO_2 as carrier gases.

Afterwards, the CO_2 isothermal products (~40 mg) were characterized to identify and quantify the products. The samples were analyzed using XRD, infrared spectroscopy (FTIR), and thermogravimetric analysis (TGA). XRD characterization was performed as described above. For FTIR spectroscopy samples were analyzed in an Alpha-Platinum spectrometer from Bruker, using the ATR mode. The TG measurements were performed under a nitrogen atmosphere using a TA Instruments model Q500HR thermobalance from 30 to 930 °C at a rate of 5 °C min^{-1}. Additionally, to elucidate if these products presented changes in their microstructural characteristics, the isothermal products were analyzed *via* N_2 adsorption–desorption and scanning electron microscopy (SEM) using the same methods described above.

Since the thermodynamic properties of the Li_2CuO_2 are not available in the literature, we performed the *ab initio* thermodynamics calculations on these CO_2 capture reactions by Li_2CuO_2 based on combining density functional theory (DFT) with lattice phonon dynamics. The detailed descriptions of the calculation method can be found in previous studies.[50–52] The CO_2 and/or H_2O capture reactions of Li_2CuO_2 can be expressed generically in the form (for convenient description, we normalized the reaction to 1 mole of CO_2 or H_2O):

$$\sum_{R_i} n_{R_i} \mathrm{Solid}R_i + CO_2 + H_2O \leftrightarrow \sum_{P_j} n_{P_j} \mathrm{Solid}P_j \qquad (1)$$

where n_{R_i}, n_{P_j} are the reagents (R_i) and products (P_j) moles involved in the capture reactions. We treat the gas phase CO_2 or H_2O as an ideal gas. By assuming that the difference between the Gibbs free energy (ΔG^0) of the solid phases of reactants (R_i) and products (P_j) can be approximated by the difference in their total energies (ΔE_{DFT}), obtained directly from DFT calculations, and the vibrational free energy of the phonons and by ignoring the PV contribution terms for solids, the variation of the Gibbs

free energy for reaction with temperature and pressure can be written as:

$$\Delta G(T,P) = \Delta G^0(T) - RT \ln \frac{P_{gas}}{P_0} \quad (2)$$

where,

$$\Delta G^0(T) \approx \Delta E_{DFT} + \Delta E_{ZP} + \Delta F_{PH}(T) - G^0_{gas}(T) \quad (3)$$

Here, ΔE_{DFT} is the DFT energy difference between the reactants and products of the reaction (1), ΔE_{ZP} is the zero point energy difference between the reactants and products and can be obtained directly from phonon calculations. ΔF_{PH} is the phonon free energy change excluding zero-point energy (which is already counted into the ΔE_{ZP} term) between the solids of products and reactants. P_{gas} is the partial pressure of CO_2 or H_2O in the gas phase and P_0 is the standard state reference pressure taken to be 1 bar. The heat of reaction ($\Delta H^{cal}(T)$) can be evaluated through the following equation:

$$\Delta H^{cal}(T) = \Delta G^0(T) + T[\Delta S_{PH}(T) - S_{gas}(T)] \quad (4)$$

where, $\Delta S_{PH}(T)$ is the difference of entropies between product solids and reactant solids. The free energy of CO_2 or H_2O (G^0_{gas}) can be obtained from standard statistical mechanics,[51–53] and its entropy (S_{gas}) can be found in the empirical thermodynamic databases.[54] The DFT calculations with plane-wave basis sets and pseudopotential approximation were done to describe the structural, energetic and electronic properties of solids considered in this study. All calculations were performed using the Vienna *ab initio* simulation package (VASP).[55,56] In this study, the PAW pseudo-potentials and PW91 exchange–correlation functional were used in all of the calculations. Plane wave basis sets were used with a kinetic energy cutoff of 520 eV and an augmentation charge cutoff of 605.4 eV. The *k*-point sampling grids of $m \times n \times l$, obtained using the Monkhorst–Pack method,[57] are used for these bulk calculations, where m, n, and l are determined with a spacing of about 0.028 $Å^{-1}$ along the reciprocal axes of their unit cells. In the phonon calculations, for each generated supercell, the displacements of 0.03 Å of non-equivalent atoms were generated. Then, for each supercell, the DFT calculations were performed again to obtain the force on each atom due to the displacements. These forces are carried back to PHONON package[58] to calculate the phonon dispersions and densities from which the partition function can be carried out and used to obtain free energies and entropies as shown in eqn (3) and (4).

3. Results and discussion

Fig. 2 shows the XRD pattern of the Li_2CuO_2 synthesized by solid state reaction. The diffraction pattern fitted to the 00-084-1971 JCPDS file, and no other phases were detected. After the structural confirmation, the sample microstructure was analyzed by N_2 adsorption and SEM. The Li_2CuO_2 morphological characteristics are shown in the Fig. 3. The size of the Li_2CuO_2 agglomerates is around 5–15 μm, but a closer analysis

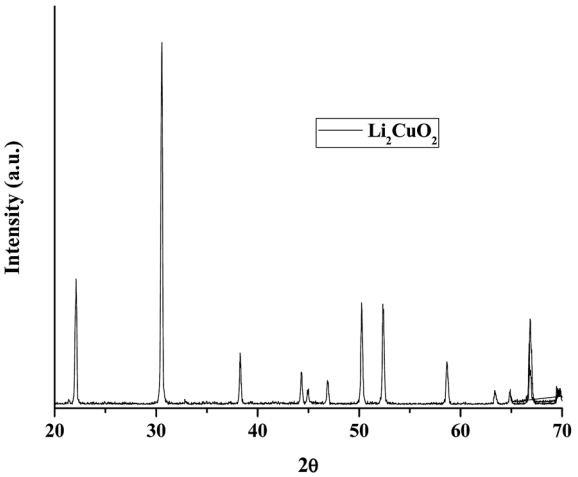

Fig. 2 X-ray diffraction pattern of the Li_2CuO_2 synthesized by solid state reaction.

indicated that these agglomerates are formed by polyhedral particles of 0.5 μm in average. Additionally, the N_2 adsorption–desorption isotherm for this sample corresponded to a type II isotherm according to the IUPAC classification (data shown below)[59] and the isotherm did not presented hysteresis. Additionally, the surface area of the sample was estimated to be 0.2 $m^2\ g^{-1}$ using the BET model. This behavior corresponds to a nonporous, dense aggregate of particles, which is in good agreement with the synthesis method (solid-state reaction) and SEM observations.

Experimentally, Li_2CuO_2–N_2–H_2O and Li_2CuO_2–CO_2–H_2O systems were evaluated at different temperatures (30–80 °C). The Li_2CuO_2–N_2–H_2O system was analyzed seeking for any possible reaction between lithium cuprate and water vapor. Fig. 4 shows water vapor sorption–desorption isotherms. It is clearly evident that all of the sorption isotherms corresponded to type III according to the IUPAC classification.[59] Water sorption varied as a function of the temperature, and it was not completed or limited to the increasing relative humidity section ramp (0–80% RH) because during some part of the decreasing RH section ramp (80–0% RH), the samples continued gaining weight. This effect was highly evidenced in the isotherm performed at 80 °C. Therefore, as these curves are dynamic experiments the water sorption equilibrium has not been reached. Final weight increments into the N_2–H_2O flow did not vary importantly. While the Li_2CuO_2 sample treated at 40 °C

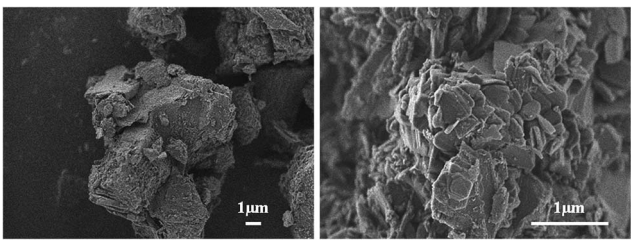

Fig. 3 Secondary electron images of the Li_2CuO_2 sample.

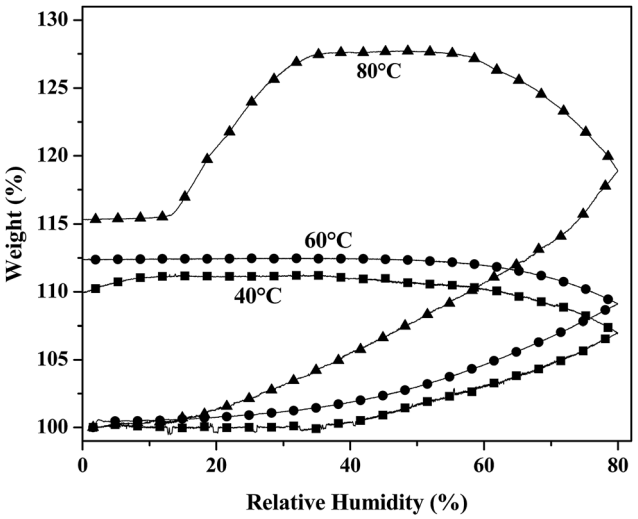

Fig. 4 Li_2CuO_2–N_2–H_2O sorption–desorption curves where different weight increments are shown as a function temperatures (40–80 °C).

gained 10.3 wt%, the final weight increment at 80 °C was 15.5 wt%. However, the sorption process began at a much lower RH when temperature was increased. At 40 °C, the weight increased at around 38% of RH, while the sorption process began with 14% of RH at 80 °C. It must be mentioned that the weight decrement observed in the sample thermally treated at 80 °C during the desorption process between 35 and 14 wt% must be attributed to water evaporation. In previous works, the final weight increments observed during the N_2–H_2O flow experiments has been attributed to a surface hydroxylation process, where different species are produced.[35–39]

Fig. 5 shows the Li_2CuO_2–CO_2–H_2O sorption–desorption curves. Again, the sorption curves were type III, as in the previous case, but the water desorption process and the final weight increments were noticeably different. In all these cases,

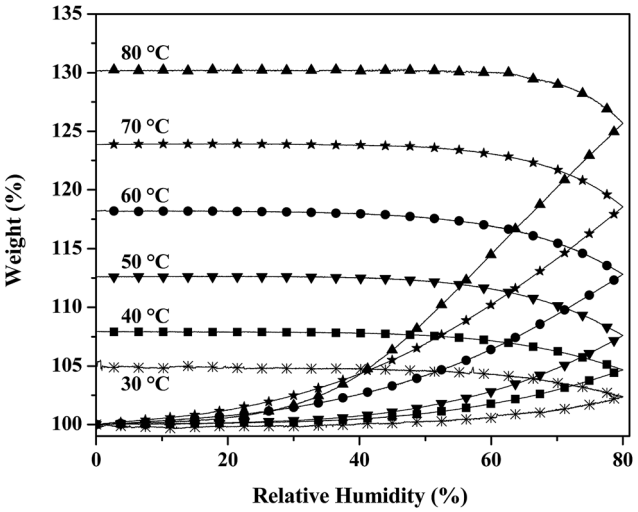

Fig. 5 Li_2CuO_2–CO_2–H_2O sorption–desorption curves where different weight increments are shown as a function temperatures (30–80 °C).

the weight gain increased as a function of the temperature, from 4.9 to 30.2 wt% at 30 and 80 °C, respectively. It means that the final weight gained is twice larger in the CO_2–H_2O system (at 80 °C) in comparison to the N_2–H_2O case. Therefore, the CO_2–H_2O system produces different reactions than N_2–H_2O, where hydration, hydroxylation, and carbonation processes must be performed.

Table 1, Fig. 6 and 7 show the calculated thermodynamic properties of CO_2 reactions with Li_2CuO_2 and LiOH (reactions (5) and (7)), as well as the Li_2CuO_2 hydroxylation reaction (reaction (6)), because lithium hydroxide seems to be the real responsible of the CO_2 capture under humidity conditions.

$$Li_2CuO_2 + CO_2 \rightarrow Li_2CO_3 + CuO \quad (5)$$

$$Li_2CuO_2 + H_2O \rightarrow 2LiOH + CuO \quad (6)$$

$$2LiOH + CO_2 \rightarrow Li_2CO_3 + H_2O \quad (7)$$

As shown in Fig. 6A, the heat of reactions (ΔH) involved in these three reactions, obey the Hess's law, and all of them are exothermic reactions. For example at 27 °C, the Li_2CuO_2 carbonation reaction (reaction (5)) has a ΔH value of -185 kJ mol^{-1}, whilst the Li_2CuO_2 hydroxylation and subsequent carbonation processes (reactions (6) and (7)) have ΔH values equal to -86 and -98 kJ mol^{-1}, respectively. In other words, the total ΔH value of reactions (6) and (7) is -184 kJ mol^{-1}, the alike energy required in reaction (5). The same tendency is observed in the whole temperature range. On the other hand, and according the ΔG values (Fig. 6B), the Li_2CuO_2 hydroxylation and LiOH carbonation reactions (reactions (6) and (7)) are less stable than Li_2CuO_2 direct carbonation. Thus, ΔG values indicate that Li_2CuO_2–CO_2–H_2O reaction system is stabilized as Li_2CO_3 and CuO, where H_2O simply acts as a catalytic intermediate. In other words, these thermodynamic data confirm that water acts as intermediate specie in the Li_2CuO_2–CO_2–H_2O system diminishing the activation energy of the whole reaction process.

Moreover, Fig. 7 shows T and P graphs describing where the chemical potential is equal to zero for the reactions (5)–(7), where $\Delta G = 0$. Around Li_2CuO_2–CO_2 and LiOH–CO_2 reaction lines are determined the chemisorption and desorption regions with optimal conditions because of the minimum energy costs at the respective temperature and pressure conditions. Additionally, in the Li_2CuO_2–H_2O reaction curve, the hydroxylation and dehydroxylation regions are determined. All these reactions are thermodynamically favorable over a certain range of temperatures and P_{CO_2} or P_{H_2O}, which means that under such conditions CO_2 and H_2O are thermodynamically favored to be reacted with Li_2CuO_2 or LiOH. However, it is evident that the CO_2 capture is more favored than the dehydroxylation process under the experimental conditions of temperature and CO_2 pressure. Based in the theoretical and experimental results, the most feasible reaction mechanism is the Li_2CuO_2 hydroxylation process subsequently followed by the LiOH carbonation process. Nevertheless, at standard pressures the CO_2

Table 1 The calculated thermodynamic properties of reaction of CO_2 captured by Li_2CuO_2 and LiOH comparison with Li_2O. T_1 and T_2 are the turnover temperatures of the CO_2 capture reactions at $P_{CO_2} = 0.1$ bar for post-combustion, $P_{CO_2} = 20$ bar for pre-combustion condition. For LiOH, assuming $P_{H_2O} = 1$ bar

Reactions	CO_2 wt%	ΔE^{DFT} (kJ mol^{-1})	ΔH (kJ mol^{-1})	ΔG (kJ mol^{-1})	T_1 (K)	T_2 (K)
$Li_2CuO_2 + CO_2 = Li_2CO_3 + CuO$	59.99	−190.052	−184.516	−135.359	1005	1335
$2LiOH + CO_2 = Li_2CO_3 + H_2O$	91.88	−76.659	−98.623	−97.134	H_t[a]	H_t
$Li_2CuO_2 + H_2O = 2LiOH + CuO$	—	−113.393	−85.893	−38.225	—	—
$Li_2O + CO_2 = Li_2CO_3$[b]	142.52	−204.786	−226.731	−179.261	1295	H_t

[a] H_t stands for the temperature out of the range of 1500 K. [b] Taken from ref. 51 and 63.

chemisorption in both materials (Li_2CuO_2 or LiOH) is favored over the Li_2CuO_2 hydroxylation process.

To further understand and analyze the influence of water during the CO_2 capture in Li_2CuO_2, different kinetic experiments are presented in Fig. 8, and these isothermal products were re-characterized to determine and quantify the species produced. Isothermal experiments were performed between 40 and 80 °C at different RH (20, 40, 60, and 80%). Weight increment rates and amounts increased as a function of the RH, as it could be expected. At 40 °C the samples treated with 20 and 40% of RH only increased their weights in 0.2 and 1.2 wt% after 3 h, respectively. When the RH was increased to 60 and 80%, the final weights were 9.2 and 20.5 wt%, respectively. Similar trends were observed at 60 and 80 °C. Nevertheless, the final weight increments increased as a function of temperature and RH. It can be well represented if the isotherms with 80% of RH are compared at different temperatures. The final weights in these cases were 20.5, 24.1 and 37.6 wt% at 40, 60 and 80 °C, respectively. It must be mentioned that after the experimental

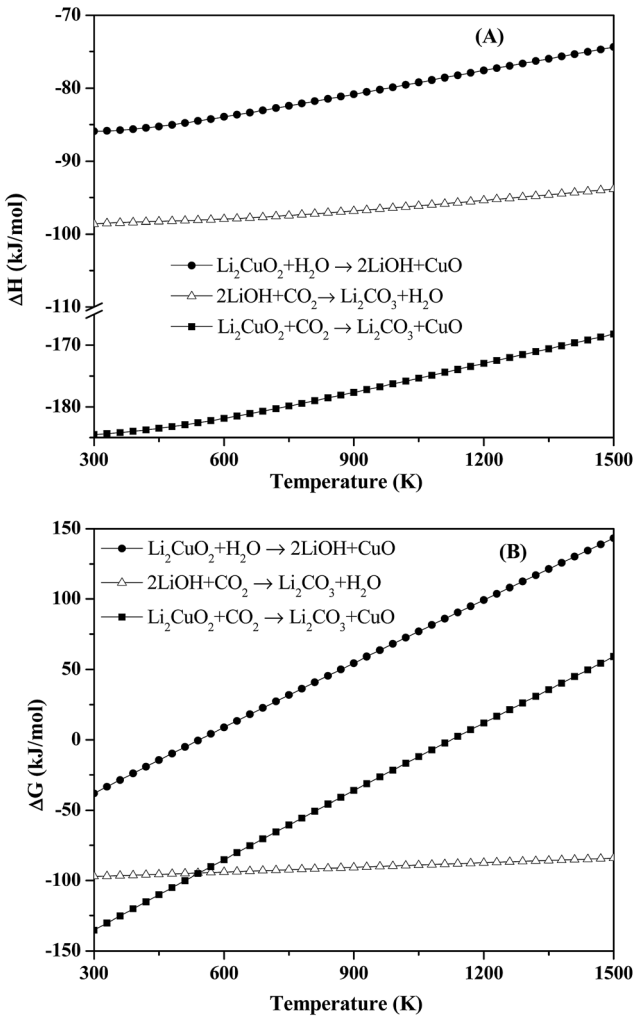

Fig. 6 The calculated thermodynamic data of different reactions of Li_2CuO_2 and LiOH capturing CO_2 *versus* temperatures, as well as the Li_2CuO_2 hydroxylation reaction: (A) heat of reaction (ΔH) and (B) free energy (ΔG).

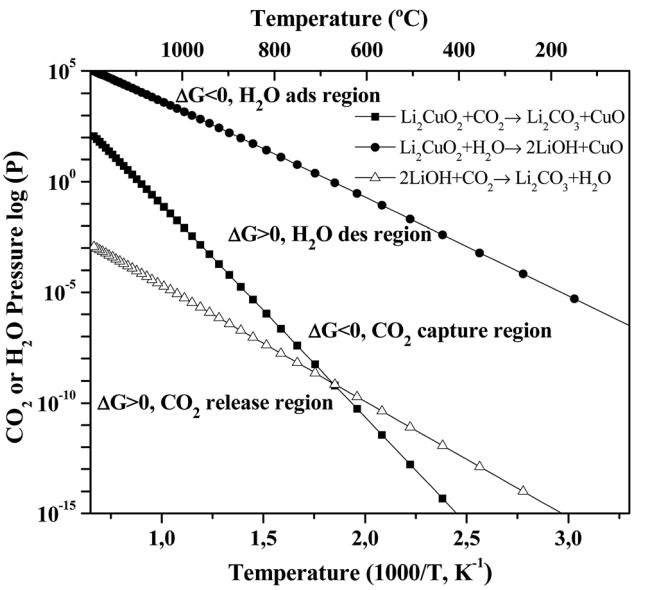

Fig. 7 The calculated vant' Hoff Plots of the relationships among the free energy (ΔG), temperature (T) and gas pressure (P in logarithmic scale). It has to be mentioned that only the $\Delta G = 0$ curves are presented here. For $Li_2CuO_2 + CO_2 = Li_2CO_3 + CuO$, $P = P_{CO_2}/P_0$, where P_0 is the reference pressure set to 1 bar; for $2LiOH + CO_2 = Li_2CO_3 + H_2O$, $P = P_{CO_2}/P_{H_2O}$. For $Li_2CuO_2 + H_2O = 2LiOH + CuO$, $P = P_{H_2O}/P_0$, where P_0 is the reference pressure set to 1 bar. For each reaction, above the curve, the sorbent absorbs CO_2 and the reaction goes forward to form Li_2CO_3, whereas below the curve, the carbonate releases CO_2 and the reaction goes backward to regenerate the sorbent.

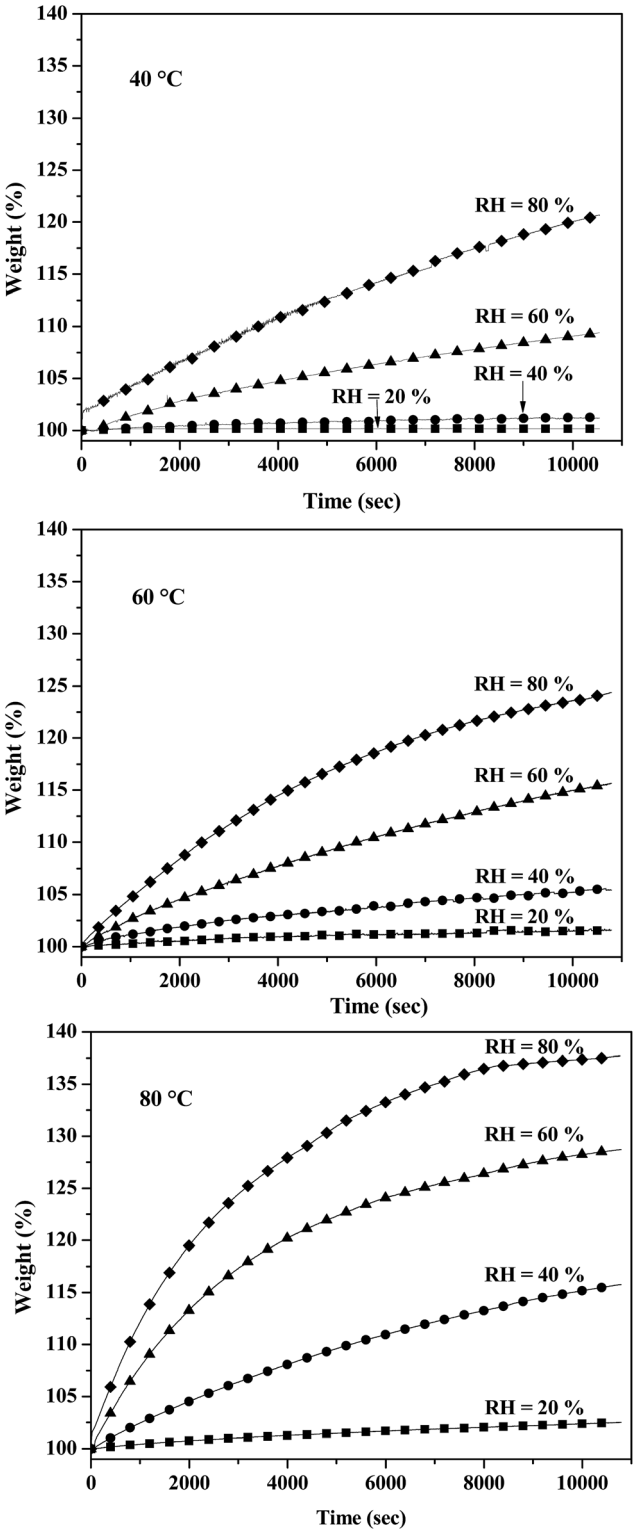

Fig. 8 Li_2CuO_2–CO_2–H_2O thermogravimetric kinetic isotherms performed at different temperatures (40, 60 and 80 °C) and RH (20, 40, 60 and 80%).

times none of these isothermal conditions reached the equilibrium. So the CO_2 capture must continue at longer times.

To confirm the CO_2 chemical capture and to quantify the CO_2 through the Li_2CO_3 formation under the different thermal and RH conditions, all the isothermal products were characterized using XRD and TGA, through decomposition thermograms. Fig. 9 shows the XRD pattern of one specific isothermal product as an example (80 °C and 80% of RH), where the CO_2 chemical capture was confirmed by the Li_2CO_3 and CuO formation (see reactions (5)–(7)). In this XRD pattern LiOH was not identified. This result strongly suggest that most of the LiOH reacted with CO_2, producing Li_2CO_3. In fact, this qualitative evidence was corroborated by the TG decomposition analysis described now. Fig. 10 shows the TG and DTG decomposition curves of isothermal products treated at 80 °C with different RH. These thermograms show three different decomposition processes. Initially, between room temperature and 120 °C, the samples lost small quantities of weight (around 1 and 2.5 wt%), which could be attributed to dehydration processes. The second weight decrement was observed between 350 and 470 °C, and it can be attributed to the dehydroxylation process. In fact, the samples treated at lower RH presented lower dehydroxylations than those observed at high HR. Additionally, the DTG dehydroxylation peaks were shifted to higher temperatures as a function of the RH, which may be related to the carbonation process. If the Li_2CO_3 shell amounts are higher, the dehydroxylation may become slower due to diffusion processes. In fact, this assumption is in good agreement with the decarbonation process, which was produced at $T \geq 600$ °C. The decarbonation process was produced in two steps between 610 and 760 °C and between 760 and 925 °C. These two processes can be described as superficial and bulk decarbonation processes. Based in these results the amounts of CO_2, trapped as Li_2CO_3 (weight lost at $T \geq 600$ °C), were quantified and plotted in Fig. 11. From these curves it is obvious that when the RH increased from 20 to 80%, the CO_2 chemisorbed increased, independently of the temperature, although the CO_2 chemisorptions at 80 °C presented the best results, where the maximum weight increment (29.5 wt%) was obtained at 80 °C and 80% of RH. This weight increment corresponds to a 72.2% of the total efficiency, although the equilibrium was not reached. So the CO_2 chemisorption may be increased as a function of time. The efficiency obtained after 3 hours

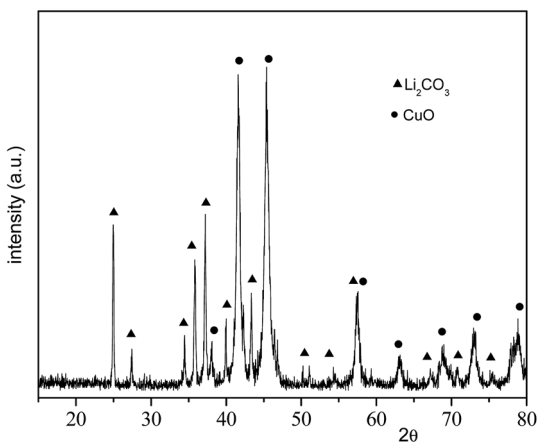

Fig. 9 XRD pattern of the Li_2CuO_2–CO_2–H_2O isothermal product treated at 80 °C with 80% of RH.

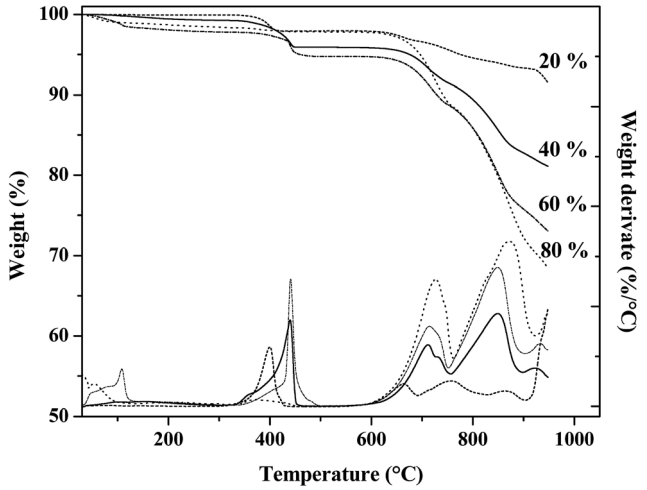

Fig. 10 TG and DTG decomposition curves of Li_2CuO_2–CO_2–H_2O products treated isothermally at 80 °C and different RH (20–80%).

corresponds to 6.7 mmoles of CO_2 per gram of Li_2CuO_2. In addition, it could be mentioned that if Li_2CuO_2 reacted totally with CO_2, the maximum theoretical CO_2 capture value would correspond to 9.13 mmoles g^{-1} (see reaction (5)).

Li_2CuO_2 and other alkaline ceramics have shown good CO_2 capture properties at moderate temperatures in the presence of water steam; in comparison to dry conditions.[35–40] The explanation given for this effect has been associated to the ceramic hydroxylation process, which promotes the CO_2 reactivity. On the other hand, different microstructural characteristics may have been modified during the CO_2 chemisorption process. So, the Li_2CuO_2–CO_2–H_2O isothermal products were analyzed by SEM and N_2 adsorption. Fig. 12 show some secondary and backscattered electron images (BSEI) of the Li_2CuO_2–CO_2–H_2O isothermal products treated at 80 °C with 80% of RH. The morphology of the sample changed importantly in comparison to the Li_2CuO_2 initial appearance (see Fig. 3). The particles seem to be still agglomerated but the polyhedral particles decreased in size importantly, from 15 μm to 200 nm. Additionally, BSEI analysis evidenced the presence of two different phases by the particle contrasts observed in the corresponding image. These two phases must correspond to Li_2CO_3 and CuO, because they are the main Li_2CuO_2 carbonation products (excluding the possible hydroxide formation). Thus, the contrast differences arise from the differences in mean atomic number ($\bar{Z}$) of Li_2CO_3 and CuO, 6 and 18.5, respectively. Therefore, the backscattered electron coefficient (η)[60] of these phases increases from 0.064 to 0.212 for Li_2CO_3 (dark phase) and CuO (light phase), respectively. From this backscattered electron image, it can be observed that CuO nanoparticles (≤200 nm) seem to be dispersed over the Li_2CO_3 phase. Finally, the N_2 adsorption–desorption isotherm of the pristine Li_2CuO_2 sample and the isothermal product treated at 80 °C and 80% of RH are presented in the Fig. 13. Both samples are isotherms type II, to the IUPAC classification,[59] but only the isothermal product presented hysteresis, H3 type. The presence of hysteresis and the large difference in the N_2 adsorbed volume clearly indicate high variations in the textural properties of these samples. Additionally, the surface areas of these samples were determined using the BET model. While the surface area of the pristine Li_2CuO_2 sample was 0.2 m^2 g^{-1}, the isothermal product had a surface area of 11.3 m^2 g^{-1}. The large difference observed between these samples may be associated Li_2CO_3–CuO external shell, which resulted to have porous and the formation of CuO nanoparticles, determined by SEM. Similar results have been published for other alkaline ceramics during the CO_2 capture.[6–34] Nevertheless, these textural modifications have been observed at much higher temperatures (450–550 °C) during the CO_2 capture process under dry conditions. In any case, the presence of porosity and/or the nanoparticles formation allows CO_2 or CO_2–H_2O diffusion, favoring the CO_2 chemisorption without the necessity of intercrystalline processes. All these results are in good agreement with the SEM and isothermal results.

All these results clearly show that CO_2 chemisorption in Li_2CuO_2 is importantly improved by the presence of water vapor in moderate temperatures (30–80 °C), in comparison to the dry conditions, as Li_2CuO_2 only chemisorbs CO_2 at higher temperatures than 250 °C under dry conditions.[46–49] If these amounts of CO_2 trapped are compared with other materials, the results seem to be highly encouraging. For example, several materials including activated carbons, zeolites, hydrotalcites, and

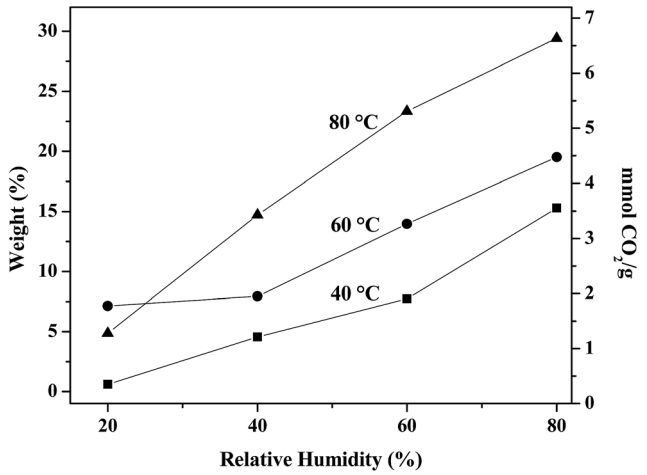

Fig. 11 Quantification of the CO_2 desorbed during the TG analyses from Li_2CO_3 by Li_2CuO_2 varying temperature and RH.

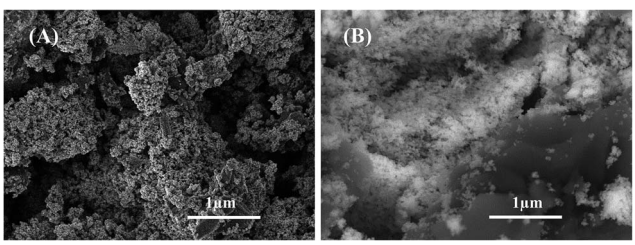

Fig. 12 Secondary (A) and backscattered (B) electron images of the Li_2CuO_2–CO_2–H_2O isothermal products treated at 80 °C with 80% of RH.

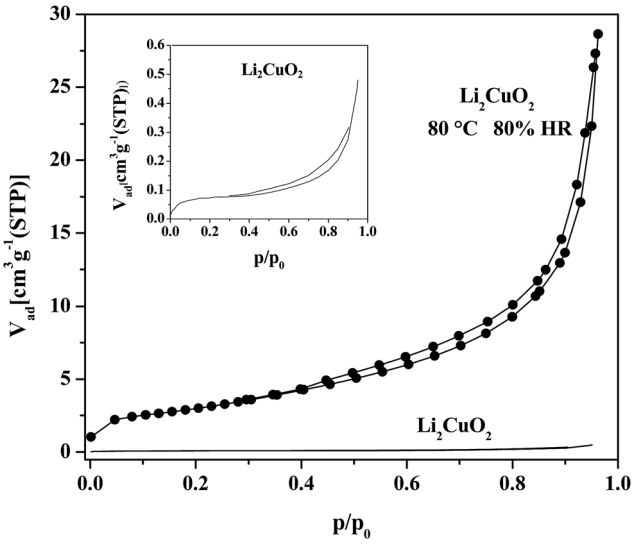

Fig. 13 N_2 adsorption–desorption isotherm of the pristine Li_2CuO_2 sample and the Li_2CuO_2–CO_2–H_2O isothermal product treated at 80 °C and 80% of RH.

amines, are able to trap, physically or chemically, around 4–6 mmoles per g in the same temperature range.[4,5,61,62] In addition, other alkaline ceramics (Li_5AlO_4 and Na_2ZrO_3, among others) tested as CO_2 captors in similar thermal and humid conditions have shown similar properties.[35–39] Nevertheless, the Li : Al molar ratio on Li_5AlO_4 is importantly higher (5 : 1) than those of Na_2ZrO_3 and Li_2CuO_2 (2 : 1). Hence, the high CO_2 chemisorption in Li_5AlO_4 at low temperatures may be attributed to the high lithium content, while in the Li_2CuO_2 case could be attributed to the high lithium accessibility presented due to its layered crystalline structure. In fact the Na_2ZrO_3 has the same alkaline : metal atomic molar ratio as well as the layered crystalline structure. Consequently, it seems that layered crystalline structures highly favor the CO_2 reactivity with Li_2CuO_2. Thus, this kind of ceramics may be considered as feasible materials for the CO_2 capture at moderate temperatures.

4. Conclusions

The Li_2CuO_2–CO_2–H_2O system was evaluated at moderate temperatures (30–80 °C). Li_2CuO_2 sample was prepared by solid-state reaction. Initial results, using N_2 as carrier gas, showed that Li_2CuO_2 traps water physically and chemically, where the water vapor adsorption and/or chemisorption depended on temperature and relative humidity. When CO_2 was used as carrier gas, important changes appeared in the results. Although Li_2CuO_2 mainly trapped CO_2 chemically, producing Li_2CO_3 and CuO. In fact, different isothermal analyses and the characterization of the isothermal products confirmed this statement. Li_2CuO_2 was able to chemisorb 6.7 mmoles of CO_2 per gram of ceramic.

Additionally, all previous results were corroborated based on the theoretical thermodynamic data for the Li_2CuO_2–CO_2, Li_2CuO_2–H_2O and LiOH–CO_2 reaction systems. ΔH and ΔG values clearly showed the different thermal stability of each reaction process at different temperature ranges, but lithium cuprate carbonation is the most plausible process at moderate temperatures. All the experimental and theoretical results showed that H_2O acts as catalytic intermediate specie, which must diminish the activation energy of the whole CO_2 chemisorption process. Thus, Li_2CuO_2 must be considered as a possible option for the CO_2 capture process at moderated or environmental temperatures.

Acknowledgements

This work was financially supported by the projects PAPIIT-UNAM (IN-102313) and SENER-CONACYT (150358). H. Lara-García thanks CONACYT for financial support. The authors thank to Adriana Tejeda and Josue Romero-Ibarra for technical help.

References

1 J. D. Figueroa, T. Fout, S. Plasynski, H. McIlvried and R. D. Srivastava, *Int. J. Greenhouse Gas Control*, 2008, **2**, 9–20.
2 J. Wang, L. Huang, R. Yang, Z. Zhang, J. Wu, Y. Gao, Q. Wang, D. O'Hare and Z. Zhong, *Energy Environ. Sci.*, 2014, **7**, 3478–3518.
3 P. Wattanaphan, T. Sema, R. Idem, Z. Liang and P. Tontiwachwuthikul, *Int. J. Greenhouse Gas Control*, 2013, **19**, 340–349.
4 S. Choi, J. Drese and C. Jones, *ChemSusChem*, 2009, **2**, 796–854.
5 S. D. Kenarsari, D. Yang, G. Jiang, S. Zhang, J. Wang, A. G. Russell, Q. Wei and M. Fan, *RSC Adv.*, 2013, **3**, 22739–22773.
6 Y. Duan, D. Luebke and H. Pennline, *Int. J. Clean Coal Energy*, 2012, **1**, 1–11.
7 P. V. Subha, B. N. Nair, P. Hareesh, A. P. Mohamed, T. Yamaguchi, K. G. K. Warrier and U. S. Hareesh, *J. Mater. Chem A*, 2014, **2**, 12792–12798.
8 J. Ida and J. Y. S. Lin, *Environ. Sci. Technol.*, 2003, **37**, 1999–2004.
9 H. Pfeiffer, C. Vazquez, V. H. Lara and P. Bosch, *Chem. Mater.*, 2007, **19**, 922–926.
10 A. Iwana, H. Stephensonb, W. Ketchiec and A. Lapkin, *Chem. Eng. J.*, 2009, **146**, 249–258.
11 E. Ochoa-Fernández, M. Rønning, T. Grande and D. Chen, *Chem. Mater.*, 2006, **18**, 1383–1385.
12 L. Martínez-dlCruz and H. Pfeiffer, *Ind. Eng. Chem. Res.*, 2010, **49**, 9038–9042.
13 Q. Xiao, Y. Liu, Y. Zhong and W. Zhu, *J. Mater. Chem.*, 2011, **21**, 3838–3842.
14 I. Alcérreca-Corte, E. Fregoso-Israel and H. Pfeiffer, *J. Phys. Chem. C*, 2008, **112**, 6520–6525.
15 L. Martínez-dlCruz and H. Pfeiffer, *J. Phys. Chem. C*, 2012, **116**, 9675–9680.
16 B. Alcántar-Vázquez, C. Diaz, I. C. Romero-Ibarra, E. Lima and H. Pfeiffer, *J. Phys. Chem. C*, 2013, **117**, 16483–16491.

17 T. Zhao, E. Ochoa-Fernández, M. Ronning and D. Chen, *Chem. Mater.*, 2007, **19**, 3294–3301.
18 L. Martínez-dlCruz and H. Pfeiffer, *J. Solid State Chem.*, 2013, **204**, 298–304.
19 B. Alcántar-Vázquez, J. F. Gómez-García, G. Tavizon, I. A. Ibarra, C. Diaz, E. Lima and H. Pfeiffer, *J. Phys. Chem. C*, 2014, **118**, 26212–26218.
20 T. Ávalos-Rendón, J. Casa-Madrid and H. Pfeiffer, *J. Phys. Chem. A*, 2009, **113**, 6919–6923.
21 X. Jiao, H. Li, L. Li, F. Xiao, N. Zhao and W. Wei, *RSC Adv.*, 2014, **4**, 47012–47020.
22 V. Mejia-Trejo, E. Fregoso-Israel and H. Pfeiffer, *Chem. Mater.*, 2008, **20**, 7171–7176.
23 C. Gauer and W. Heschel, *J. Mater. Sci.*, 2006, **41**, 2405–2409.
24 R. Rodríguez-Mosqueda and H. Pfeiffer, *J. Phys. Chem. A*, 2010, **114**, 4535–4541.
25 M. Kato, K. Nakagawa, K. Essaki, Y. Maezawa, S. Takeda, R. Kogo and Y. Hagiwara, *Int. J. Appl. Ceram. Technol.*, 2005, **2**, 467–475.
26 M. Kato, S. Yoshikawa and K. Nakagawa, *J. Mater. Sci. Lett.*, 2002, **21**, 485–487.
27 S. Wang, C. An and Q. H. Zhang, *J. Mater. Chem. A*, 2013, **1**, 3540–3550.
28 T. Okumura, K. Enomoto, N. Togashi and K. Oh-Ishi, *J. Ceram. Soc. Jpn.*, 2007, **115**, 491–497.
29 K. Essaki, K. Nakagawa, M. Kato and H. Uemoto, *J. Chem. Eng. Jpn.*, 2004, **37**, 772–777.
30 K. Essaki, M. Kato and H. Uemoto, *J. Mater. Sci.*, 2005, **18**, 5017–5019.
31 S. Y. Shan, Q. M. Jia, L. H. Jiang, Q. C. Li, Y. M. Wang and J. H. Peng, *Ceram. Int.*, 2013, **39**, 5437–5441.
32 Z. Qi, H. Daying, L. Yang, Y. Qian and Z. Zibin, *AIChE J.*, 2013, **59**, 901–911.
33 S. Kumar and S. K. Saxena, *Mater. Renew. Sustain. Energy*, 2014, **3**, 30.
34 J. Fagerlund, J. Highfield and R. Zevenhoven, *RSC Adv.*, 2012, **2**, 10380–10393.
35 L. Martinez-dlCruz and H. Pfeiffer, *J. Phys. Chem. C*, 2010, **114**, 9453–9458.
36 G. G. Santillan-Reyes and H. Pfeiffer, *Int. J. Greenhouse Gas Control*, 2011, **5**, 1624–1629.
37 J. Ortiz-Landeros, C. Gomez-Yañez and H. Pfeiffer, *J. Solid State Chem.*, 2011, **184**, 2257–2262.
38 T. Ávalos-Rendon and H. Pfeiffer, *Energy Fuels*, 2012, **26**, 3110–3114.
39 R. Rodríguez-Mosqueda and H. Pfeiffer, *J. Phys. Chem. C*, 2013, **117**, 13452–13461.
40 S. Zhang, Q. Zhang, H. Wang, Y. Ni and Z. Zhu, *Int. J. Hydrogen Energy*, 2014, **39**, 17913–17920.
41 E. M. L. Chung, G. J. McIntyre, D. M. Paul, G. Balakrishnan and M. R. Lees, *Phys. Rev. B: Condens. Matter Mater. Phys.*, 2003, **68**, 144410.
42 A. S. Prakash, D. Larcher, M. Morcrette, M. S. Hegde, J.-B. Leriche and C. Masquelier, *Chem. Mater.*, 2005, **17**, 4406–4415.
43 G. Vitins, E. A. Raekelboom, M. T. Weller and J. R. Owen, *J. Power Sources*, 2003, **119–121**, 938–942.
44 K. Nakamura, K. Kawai, K. Yamada, Y. Michihiro, T. Moriga, I. Nakabayashi and T. Kanashiro, *Solid State Ionics*, 2006, **177**, 2775–2778.
45 F. Sapina, J. Rodriguez-Carvajal, M. J. Sanchis, R. Ibanez, A. Beltran and D. Beltran, *Solid State Commun.*, 1990, **74**, 779–784.
46 L. M. Palacios-Romero and H. Pfeiffer, *Chem. Lett.*, 2008, **37**, 862–863.
47 L. M. Palacios-Romero, E. Lima and H. Pfeiffer, *J. Phys. Chem. A*, 2009, **113**, 193–198.
48 Y. Matsukura, T. Okumura, R. Kobayashi and K. Oh-ishi, *Chem. Lett.*, 2010, **39**, 966–967.
49 K. Oh-ishi, Y. Matsukura, T. Okumura, Y. Matsunaga and R. Kobayashi, *J. Solid State Chem.*, 2014, **211**, 162–169.
50 Y. Duan, H. Pfeiffer, B. Y. Li, I. C. Romero-Ibarra, D. C. Sorescu, D. R. Luebke and J. W. Halley, *Phys. Chem. Chem. Phys.*, 2013, **15**, 13538–13558.
51 Y. Duan and D. C. Sorescu, *Phys. Rev. B: Condens. Matter Mater. Phys.*, 2009, **79**, 014301.
52 Y. Duan and D. C. Sorescu, *J. Chem. Phys.*, 2010, **133**, 074508.
53 B. Zhang, Y. Duan and J. K. Johnson, *J. Chem. Phys.*, 2012, **136**, 064516.
54 M. W. J. Chase, NIST-JANAF Themochemical Tables, *Journal of Physical and Chemical Reference Data*, Monograph, 4th edn, 1998, vol. 9, 1 1951.
55 G. Kresse and J. Hafner, *Phys. Rev. B: Condens. Matter Mater. Phys.*, 1993, **47**, 558–561.
56 G. Kresse and J. Furthmuller, *Comput. Mater. Sci.*, 1996, **6**, 15–50.
57 H. J. Monkhorst and J. D. Pack, *Phys. Rev. B: Solid State*, 1976, **13**, 5188–5192.
58 K. Parlinski, Software PHONON, *Computing for Materials*, Krakow, Poland, 2006.
59 S. Lowell, J. E. Shields and M. A. Thomas, *Particle Technology Series*, Kluwer Academic Publishers, London, 2004.
60 H. Pfeiffer and K. Knowles, *J. Eur. Ceram. Soc.*, 2004, **24**, 2433–2443.
61 Q. Wang, J. Luo, Z. Zhong and A. Borgna, *Energy Environ. Sci.*, 2011, **4**, 42–55.
62 D. A. Torres-Rodríguez, E. Lima, J. S. Valente and H. Pfeiffer, *J. Phys. Chem. A*, 2011, **115**, 12243–12250.
63 Y. Duan, B. Zhang, D. C. Sorescu and J. K. Johnson, *J. Solid State Chem.*, 2011, **184**, 304–311.